



Numerical simulation of the peculiar subsonic flow-field about the VFE-2 delta wing with rounded leading edge[☆]

Willy Fritz¹

EADS Military Air Systems, 85077 Manching, Germany

ARTICLE INFO

Article history:

Available online 20 February 2012

Keywords:

Vortical flow
Delta wing
Round leading edge
Numerical simulation

ABSTRACT

The Second International Vortex Flow Experiment provided a variety of experimental data for a 65° swept delta wing sharp and blunt leading edges. Flow details including forces and moments, surface pressures, Pressure Sensitive Paint measurements, and off-surface flow variables from Particle Image Velocimetry were made available for comparisons with computational simulations. This paper concentrates on some typical problems of delta wings with rounded leading edges at subsonic speed: the prediction of the main leading edge separation, the generation of the second inner vortex, the effect of transition, and Reynolds number effects.

© 2012 Elsevier Masson SAS. All rights reserved.

1. Introduction

First International Vortex Flow Experiment [6] (VFE-1) has focused on a 65° swept delta wing with a sharp leading edge. This configuration generates the “classical” vortical flow field consisting of a dominating primary vortex, a weaker secondary vortex, and sometimes even of a tertiary separation. Since the mid 1980s delta wing flow fields are simulated using Reynolds-Averaged Navier–Stokes (RANS) methods, first with algebraic turbulence models, later with 1- and 2-equation turbulence models (see [7] for example). In recent time hybrid turbulence models have also been applied to the flow around delta wings with good success [23]. Together with carefully generated grids, RANS methods are able to predict the flow features over a wide range very well. Two problem areas are however remaining: vortex break down, and the region of the secondary vortex. Vortex break down is predicted very often at earlier angles of attack as in the experiment, and in the region of the secondary vortex there are often problems in predicting the correct strength and location of this secondary vortex. Both problems are commonly related to still existing defects of the actual turbulence models. But such defects are only concluded from the disagreement of the surface pressure data. Detailed volume data like velocity vectors, and velocity fluctuations in special cross sections, which would allow a better assessment of the turbulence model, are still rarely.

To provide the computational community with such field data was one important motivation for the Second Vortex FLOW Exper-

iment (VFE-2), as it was suggested by Hummel [13] 2001 in Loen. Another motivation was to provide improved experimental data also for delta wings with rounded leading edges. With this background, the VFE-2 was embedded into the RTO task group AVT-113 under the facet VFE-2.

Before the beginning of VFE-2 experimental results from the NASA Langley Research Center on a 65° swept delta wing were already available [2]. For one sharp and three rounded leading edges normal force and pitching moment as well as pressure distribution measurements had been carried out for a large variety of Mach numbers and Reynolds numbers. The results of these measurements have been analyzed and summarized in Refs. [18–21]. This data base has been used at EADS for an assessment of different turbulence models in a very early phase of the VFE-2, as new experimental results were not yet available. Especially the effect of the Reynolds number ($Re = 6$ Mio and $Re = 60$ Mio) on a delta wing with a more realistic round leading edge was of interest. At the end of these validation calculations first results of new VFE-2 measurements were available [11]. The PSP measurements at DLR have shown very clearly the footprint of a second primary vortex for the round leading edge test case [14]. The origin of this second primary vortex was not clear from the PSP results, but in [1] there is already given a first numerical visualization of this second vortex by Chiba and Obayashi.

So at EADS the simulation of this second primary vortex was also considered as a special assessment of the quality of the CFD tools, and some additional work towards the simulation of this peculiar flow field was done. These investigations have been concentrated on the test cases listed in Table 1.

(A complete listing of all 28 CFD test cases of VFE-2 is given in Ref. [8].) Test case 5 was used for a study of the effects of small and large variations of the Reynolds number, and of the effect of transition. The test cases 4.5 and 14 were used for a numerical

[☆] The original version of this material was first published by the Research and Technology Organization, North Atlantic Treaty Organization (RTO/NATO) in RTO Report RTO-TR-AVT-113, “Understanding and Modeling Vortical Flows to Improve the Technology Readiness Level for Military Aircraft,” in October 2009.

E-mail address: willy.fritz@eads.com.

¹ R&D Engineer, Aerodynamics and Methods, AIAA Senior Member.

Nomenclature

b	wing span
CFD	Computational Fluid Dynamics
C_p	pressure coefficient, $\equiv (p - p_\infty)/q_\infty$
c_r	root chord (also c)
d	sting diameter
M	Mach number, $\equiv V/a$
MRLE	Medium Range Leading Edge Radius
p	pressure
PSP	Pressure Sensitive Paint
SAE	Spalart Almaras turbulence model with Edwards modification
RSM	Reynolds Stress Model
Re	Reynolds number based on mean aerodynamic chord, $\equiv V_\infty c_{mac}/\nu$
r_{le}	leading edge radius

S	wing plan form area
t	wing maximum thickness
x	longitudinal dimension ($x = 0$ at apex of wing)
x_v	position of vortex origin
α	angle of attack..... °
η	normalized local half span of the wing, $\equiv 2y/b$
∞	free stream condition

Organizations

DLR	German Aerospace Center/Germany
EADS	European Aeronautic Defense and Space Company/Germany
NASA	National Aeronautics and Space Administration/United States
TUM	Technical University of Munich/Germany

Table 1
CFD test cases used in the present calculations.

Case No.	Leading edge*	Mach no., M_∞	Angle of attack, α (°)	Reynolds number, Re
4.5	MRLE	0.4	13	3×10^6
5	MRLE	0.4	13	6×10^6
14	MRLE	0.4	18	6×10^6

analysis of the peculiar flow field of the delta wing with rounded leading edge.

2. Geometry and computational grids

The geometry for the VFE-2 is a 65° swept delta wing with a flat plate inner portion and interchangeable leading edges. It has been initially tested at the NASA Langley Research Center [2,22]. Three different leading edge configurations were chosen: a sharp leading edge and three rounded leading edges of varying radii [2]. Because of the analytical geometry definition and because of its general availability it was also chosen as test case for the new experimental investigations [12,15,17,9,3]. Fig. 1 shows this geometry. The configuration was used with sharp and medium range rounded leading edge (which is generally referred as round leading edge within VFE-2) for all new experiments and also for the numerical calculations [10,24,5,4,25] within VFE-2.

Because of the very simple geometry, a structured approach was used for the numerical simulations at EADS. This allows the generation of well tailored, rather orthogonal grids which minimize the numerical discretization error. The grids have been generated by an in-house developed hyperbolic grid generator which runs automatically and allows the generation of grids with 10 million grid points within several minutes. The grid structure is shown in Fig. 2. The grid is a so-called conical C–O type mesh. This grid type has proven to be very suitable for vortical flow in numerous calculations. It has a singular line from the wing apex to the upstream far field boundary. The sting is kept with constant diameter until to the downstream far field boundary. Close to the surface and around the round leading edge, the grid lines are nearly orthogonal. The grid is build up by 321 points in stream wise direction (starting from the wing apex, and 257 point aligned with the wing surface), 257 points in circumferential direction, and 129 points normal to the wing surface. This results in a total number of 10.6 million grid points. The grid is subdivided into 24 blocks for use of the flow solver in parallel mode.

3. Flow solver

The DLR flow solver FLOWer [16] has been used for the RANS calculations at EADS. The FLOWer code is designed for applica-

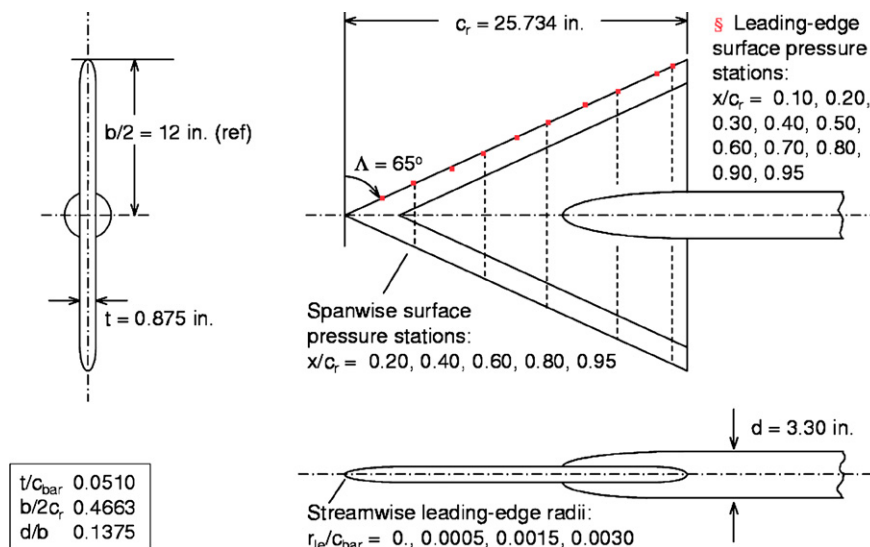


Fig. 1. Geometry of VFE-2 delta wing; Ref. [2].

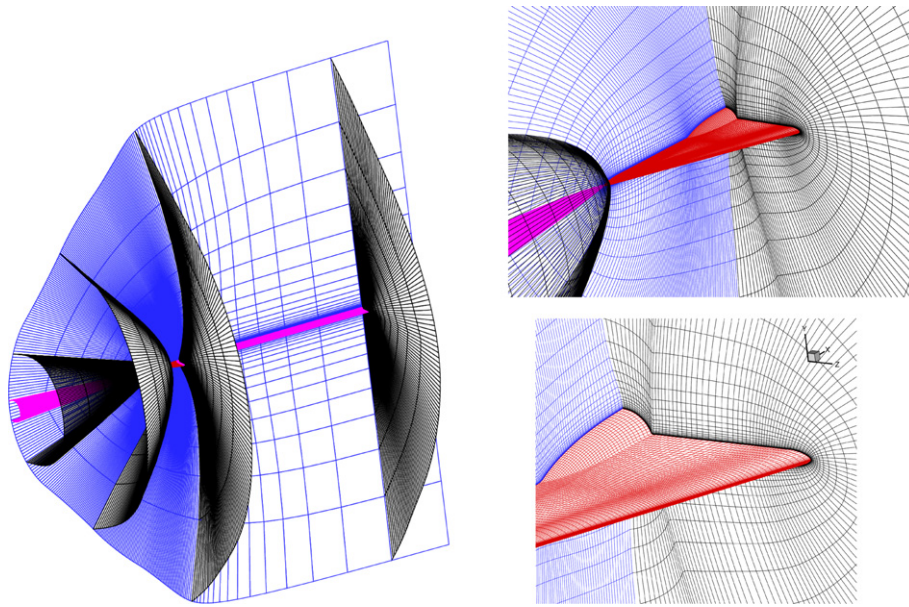


Fig. 2. 3-D grid structure (only each second line in each direction is shown).

tion on multi-block grids and has been operated in a Jameson-type mode as a cell-vertex explicit multi-grid scheme using a finite volume approach and a Runge–Kutta type scheme with central differences in space for the time integration. The numerical dissipation model is the anisotropic dissipation model of Jameson, where the dissipation terms are scaled with the relations of the convective eigenvalues in each direction of the control volume. Additionally the dissipative flux vector is optimized by a relaxation between old and new values within the Runge–Kutta scheme.

Convergence acceleration has been achieved by local time stepping, implicit residual smoothing and by use of the full multi-grid strategy (3-level W-cycle). For further reduction of computing time, FLOWer was run on 24 processors on a Linux cluster. Depending on the flow features, 2000–4000 multi-grid cycles were necessary for a converged solution.

In the RANS mode, FLOWer offers a variety of different one- and two equation turbulence models and also several Reynolds Stress models. The calculations have been performed using the SAE-model, the Wilcox $k-\omega$ model, and the RSM model, but all the following results were obtained with the Wilcox $k-\omega$ model.

For all the different turbulence models, FLOWer has the option to specify transition. This option was used in some calculations by specifying transition along a conical line along the upper side of the wing. Upstream of the transition line, laminar flow is simulated by zero production in the turbulent transport equations.

4. Results and discussion

4.1. Effect of leading edge bluntness

The experimental results of the NASA Langley Research Center [2,22] offer a data base for three different round leading edges. So before starting the investigation for a delta wing with a realistic round leading edge, some general investigations at the delta wings with different leading edges have been performed at EADS. A typical result is presented in Fig. 3.

This figure shows surface pressure contours for the VFE-2 delta wing with different leading edges. The sharp leading edge (Fig. 3a) shows the typical leading edge vortex beginning at the wing apex. The wing with the small range leading edge (Fig. 3b) shows a

very similar flow pattern, the leading edge separation begins very close to the wing apex. With the large range leading edge radius (Fig. 3d) there is no leading separation, the leading edge is too blunt. The medium range leading edge radius (Fig. 3c) generates a combination of the latter two cases. In the forward part of the wing, the flow passes the round leading edge (as the absolute leading edge radius is constant, the leading edge is relative blunt in this part of the wing). By the increasing half span of the wing and the constant leading edge radius, the wing gets relatively sharper in stream wise direction. So at a certain distance of the wing apex, the flow separates and the leading edge vortex develops. This transition of the relative leading edge sharpness is very important for the understanding of the flow field about this wing. There is also the footprint of a second, inner vortex in the surface pressure contours of the wing with the medium range leading edge radius. This vortex, which makes the flow field peculiar, will be discussed in more details within this paper.

All further calculations presented in this paper will concentrate on this medium range leading edge wing, and it will be referred as VFE-2 delta wing with rounded leading edge. From an analysis of the experimental data [18,21] it is known, that increasing Re number delays, and that increasing Mach number promotes the primary separation. With increasing incidence the primary separation point moves upstream towards the wing apex.

4.2. Effect of Reynolds number and transition

The simulation of Reynolds number effect can be a very important application of the numerical simulation, as it would help very much to scale wind tunnel test data to real flight conditions. As the NASA experiments [2] offer test data for a variation of the Reynolds number from 6 million to 60 million, they have been used for first test calculations within EADS. The results are discussed in this section.

Fig. 4 shows very clearly, that the higher Reynolds number delays the leading edge separation. At the lower Reynolds number (Fig. 4a) the development of the primary vortex begins at $x/c_r \approx 0.2$, whereas at the high Reynolds number it begins somewhere between $x/c_r = 0.6$ and $x/c_r = 0.8$.

In Fig. 5 the effect of the different Reynolds numbers is shown for two different numerical calculations. The left-hand side of the

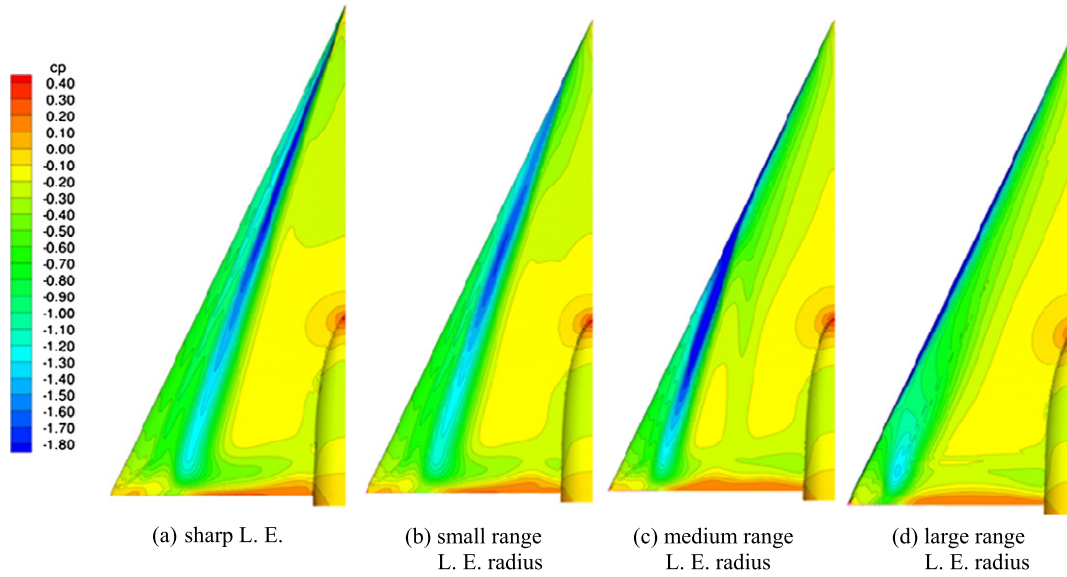


Fig. 3. Effect of leading edge bluntness, $M = 0.4$, $Re = 6 \times 10^6$, $\alpha = 13^\circ$.

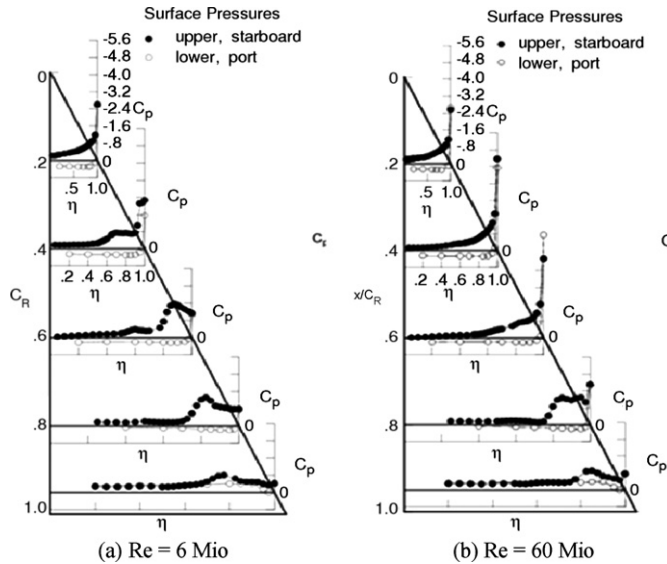


Fig. 4. Effect of large Reynolds number variation in the experiments, $M = 0.4$, $\alpha = 13^\circ$; Ref. [2].

figure shows the results for calculations without setting transition (fully turbulent, which is by default used in RANS calculation). On the right-hand side there are the results for calculations with prescribed transition along a conical line. The distance of the transition line from the leading edge is 0.003 of the local (full) wing span (0.3%). The impact of the transition setting is quite considerable. Without transition the leading edge separation at the low Re is delayed too much, and at the high Re it is promoted too much (left-hand side of Fig. 5). With transition however, the effect of the Reynolds number is matched very well and also the position of the separation points are very close to the experimental separation points. This effect of the transition setting was also observed at other turbulence models (SAE, RSM): only by prescribing transition, reasonable results were obtained at $Re = 60$ Mio, and at $Re = 6$ Mio, without transition all three turbulence models delayed the primary separation too much.

It is not quite clear, whether this is a real physical effect or only a numerical effect of the turbulence model (possibly the turbulence model produces too much eddy viscosity around the leading edge, which then is corrected by forcing laminar flow in this region). As long as no experimental data about transition locations or effects of different transition locations are available, the transition setting at 0.3% is arbitrary, but it shows, how sensitive to small

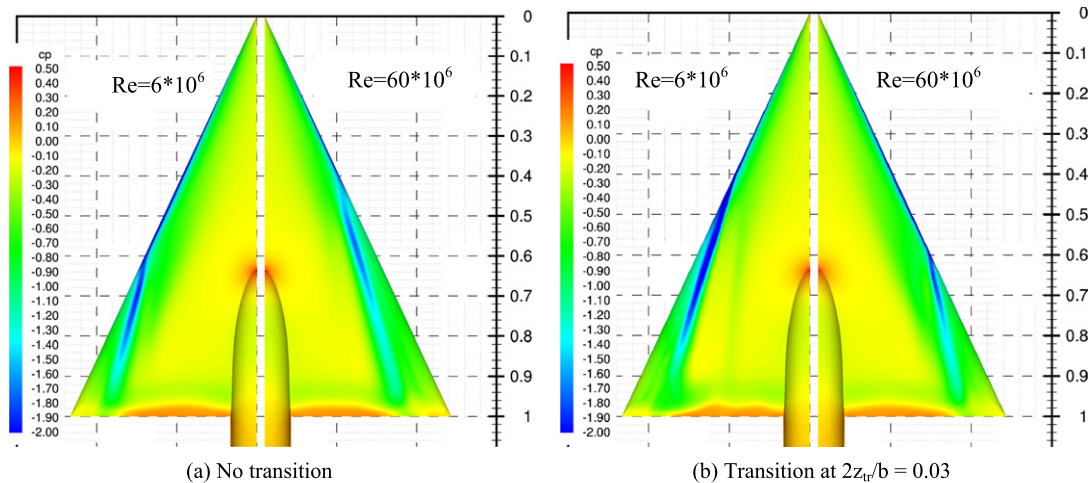


Fig. 5. Effect of large Reynolds number variation in the calculations (RANS, Wilcox $k-\omega$), $M = 0.4$, $\alpha = 13^\circ$.

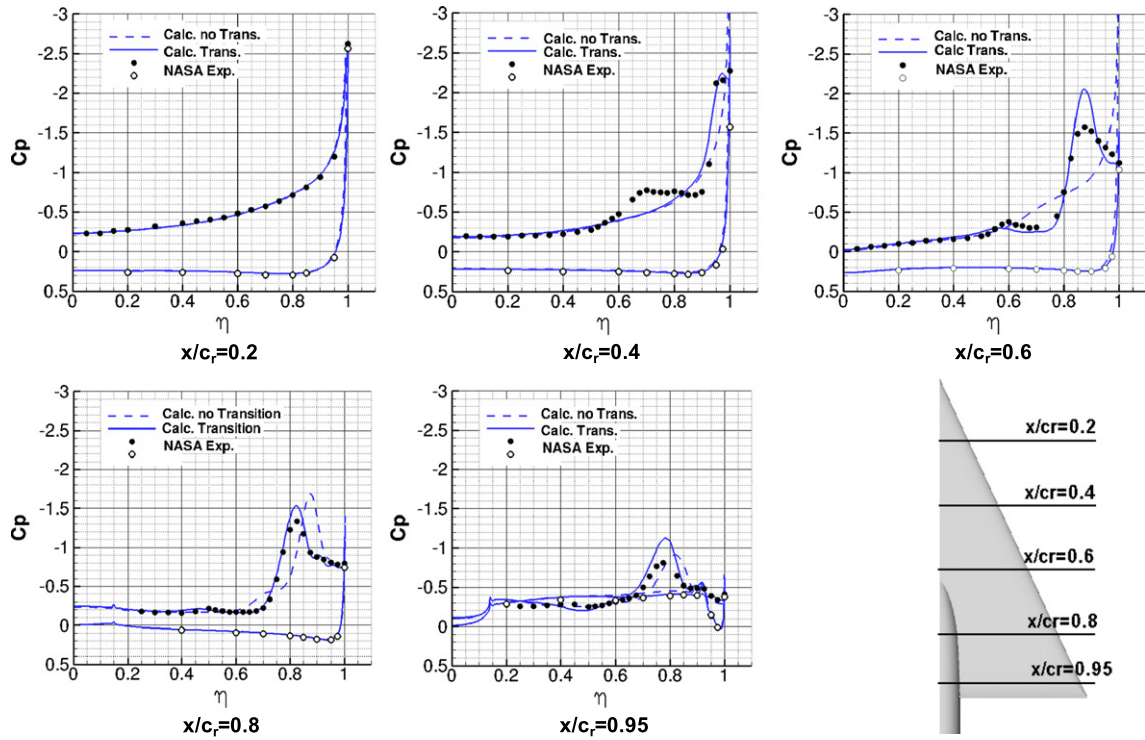


Fig. 6. Comparisons of surface pressure with experiments for $M = 0.4$, $Re = 6 \text{ Mio}$, $\alpha = 13^\circ$. With and without transition.

variations this primary separation is. The position of this separation point has of course great impact on the local surface pressure distribution as Fig. 6 illustrates.

With the specified transition, the experimental data are fitted quite well, whereas the calculation without transition shows a too much delayed leading edge separation. This investigation shows very clearly, that the correct prediction of the primary separation for a round leading edge is a very difficult task and very sensitive to small variations of the eddy viscosity (and by this of course also to numerical viscosity). At very high Reynolds numbers this sensitivity seems to be much stronger. As the setting of the transition at 0.03% local half span is rather arbitrary (this value was found after some trials to fit best the experiments), and as long as there are no physical reasons to do this, the transition setting has only been used for this investigation in order to demonstrate the impact of it. All further calculations have been done without transition.

At least for small variations of the Reynolds number the fully turbulent RANS solution shows the correct effect of the Re variation as it can be seen in Fig. 7. The leading edge separation is now delayed by the increasing Reynolds number, but compared with the experiments too much (see Fig. 6). So it can be concluded that the effects of Reynolds number variations which are of interest within this paper ($Re = 1 \text{ Mio}$, $Re = 2 \text{ Mio}$, $Re = 3 \text{ Mio}$, $Re = 6 \text{ Mio}$) are prescribed qualitatively correct by fully turbulent RANS simulations.

The surface pressure contours of the numerical solution for $Re = 3 \text{ Mio}$ are very similar to the corresponding surface pressure contours of the DLR PSP experiments [15], as it is shown in Fig. 8. This case is the famous test case 4.5 within the VFE-2 and will be investigated in more details in the next section.

4.3. Test case 4.5, $M = 0.4$, $Re = 3 \times 10^6$, $\alpha = 13^\circ$

Fig. 8 shows the comparison of the surface pressure contours from the numerical solution and from the DLR PSP experiment [15]. Obviously the separation point of the primary vortex is

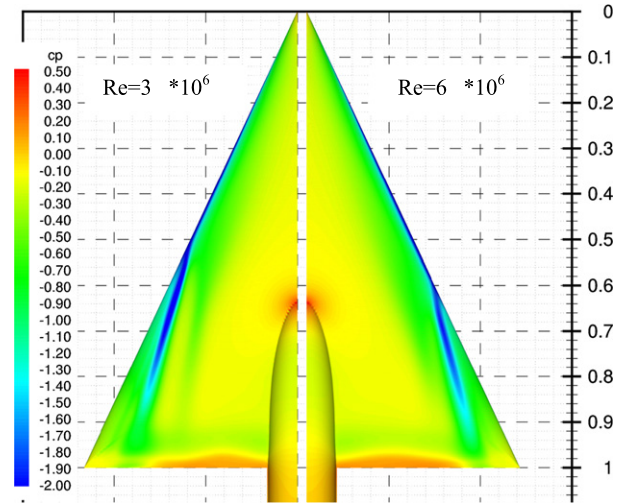


Fig. 7. Effect of a small Reynolds number variation in the calculation. (RANS, Wilcox $k-\omega$), $M = 0.4$, $\alpha = 13^\circ$.

very close to the experimental separation point for this test case. Both surface pressure contours show very clearly the footprint of this second inner vortex. There is a rather compact suction peak at the beginning of this secondary vortex in the experiment. In the numerical result this suction peak is not present, the pressure contours are smoother, but besides this, both pressure contours are rather similar.

The main flow features for this test case are really well predicted by the RANS solution as Fig. 9 underlines. The second vortex is at the correct position, but compared to the experiment it is too weak. The primary vortex is matched very well. At the cross section $x/c_r = 0.8$ there can be seen the typical problem of RANS: deficits in the pressure prediction in the region of the secondary vortex. The experimental data are not fitted exactly, but due to the

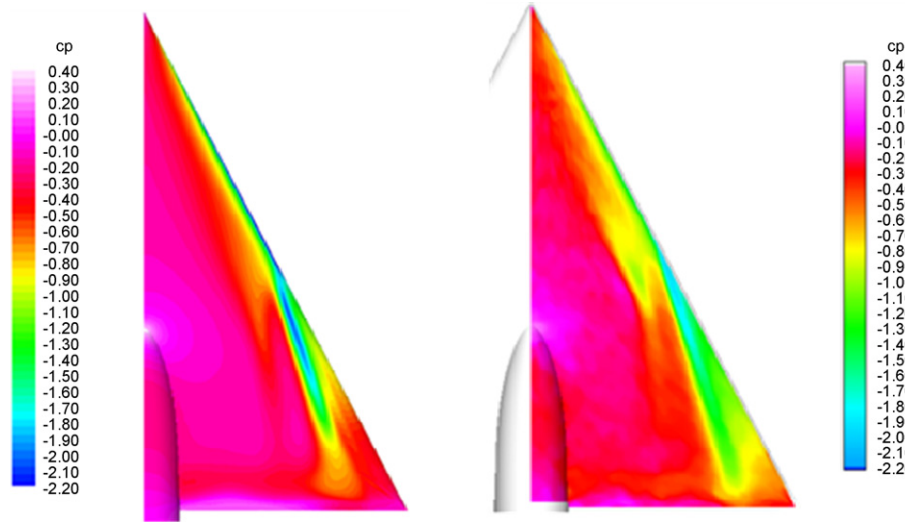


Fig. 8. Comparison of numerical and experimental surface pressure contours for case 4.5 ($M = 0.4$, $Re = 3 \times 10^6$, $\alpha = 13^\circ$).

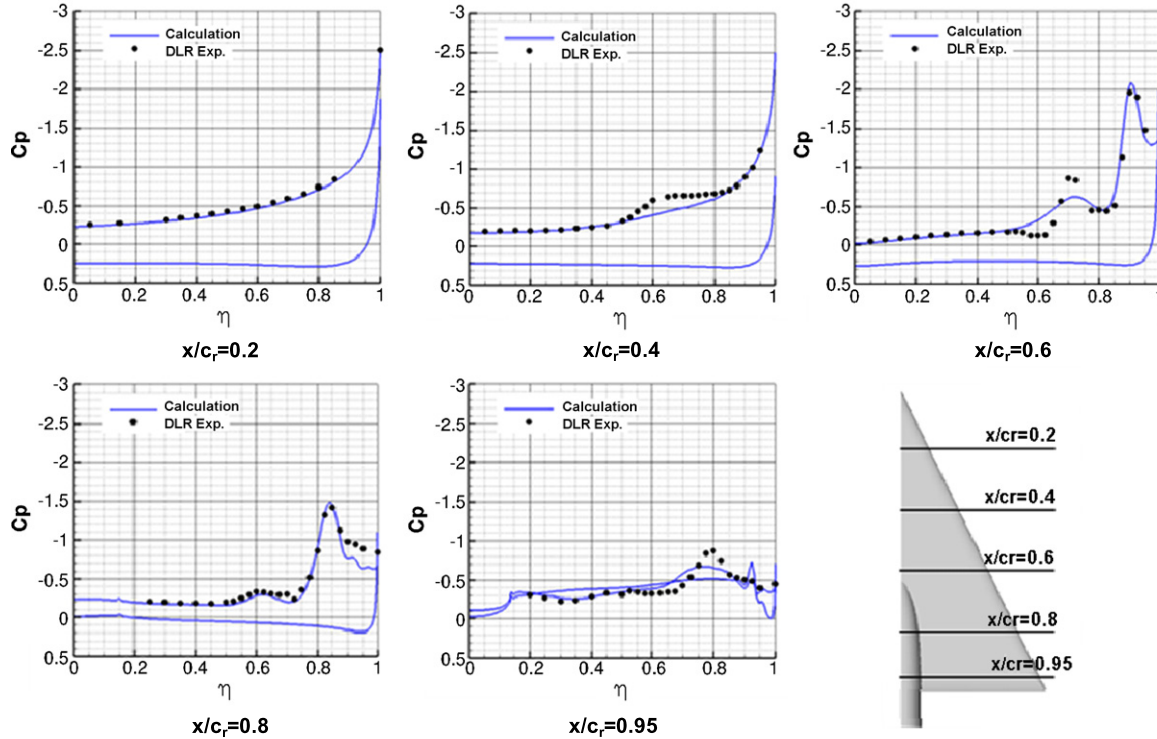


Fig. 9. Comparison of numerical and experimental surface pressure distributions for case 4.5 ($M = 0.4$, $Re = 3 \times 10^6$, $\alpha = 13^\circ$).

good agreement of the overall flow features, the CFD data can be used for an analysis about the origin of this second vortex.

Fig. 10 gives a first impression about the origin of this inner vortex. The iso-surface of 5% total pressure loss indicates an already separated, thick boundary layer in the apex region of the wing. Possibly by the leading edge suction this thick and rotating boundary layer is sucked towards the leading edge. Thus it gets thicker and then finally rolls up to this inner vortex. As soon as the main leading edge separation sets on, all separated flow material is fed into this primary vortex, which consequently grows up in stream wise direction.

The total pressure loss contours in different cross sections, which are shown in Fig. 11, give an impression about the dimension of this inner vortex. It is nearly as big as the main primary vortex, but much weaker. It is not fed by the leading edge therefore

it gets weaker in downstream direction. At the very beginning this inner vortex also induces a secondary vortex. Fig. 11 also shows that the leading edge vortex follows the leading edge, whereas the inner vortex is more parallel to the main flow direction.

The velocity vectors in Fig. 12 show that already in the very forward region of the wing ($x/c_r = 0.2$) there is a thin separated region. The total pressure loss contours (the range from 2% blue, to 24% red) indicate, that this separated region becomes thicker and stronger in stream wise direction. (The close-up range and the length scale of the velocity vectors is not identical in both pictures, it has been chosen such that details can be seen, and not all vectors are shown.)

At $x/c_r = 0.5$ (left-hand side of Fig. 13) the separated region is already very thick, but it is still growing continuously from the leading edge towards the inner part of the wing. At $x/c_r = 0.55$,

the leading edge separation sets on and the separated region now grows much faster close to the leading edge. More inboard, the thick boundary layer gradually forms a flat vortex.

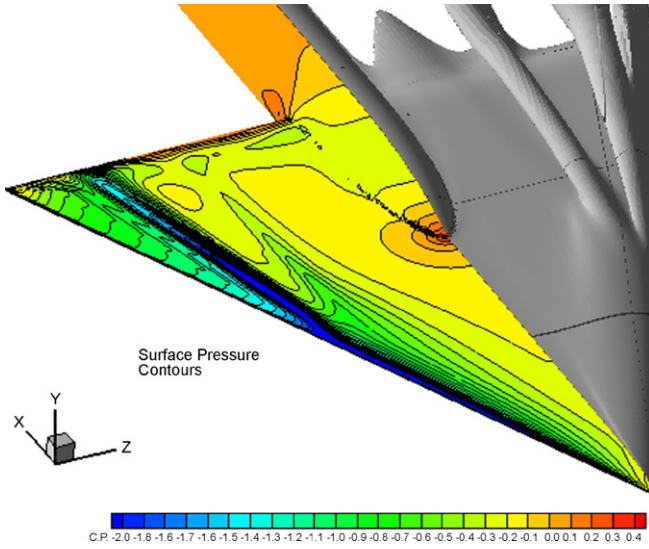


Fig. 10. Surface pressure contours and iso-surface of 5% total pressure loss for case 4.5 ($M = 0.4$, $Re = 3 \times 10^6$, $\alpha = 13^\circ$).

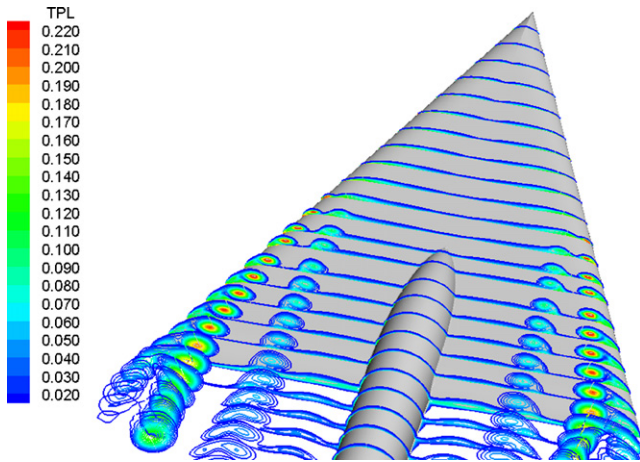


Fig. 11. Total pressure loss contours in different cross sections for case 4.5 ($M = 0.4$, $Re = 3 \times 10^6$, $\alpha = 13^\circ$).

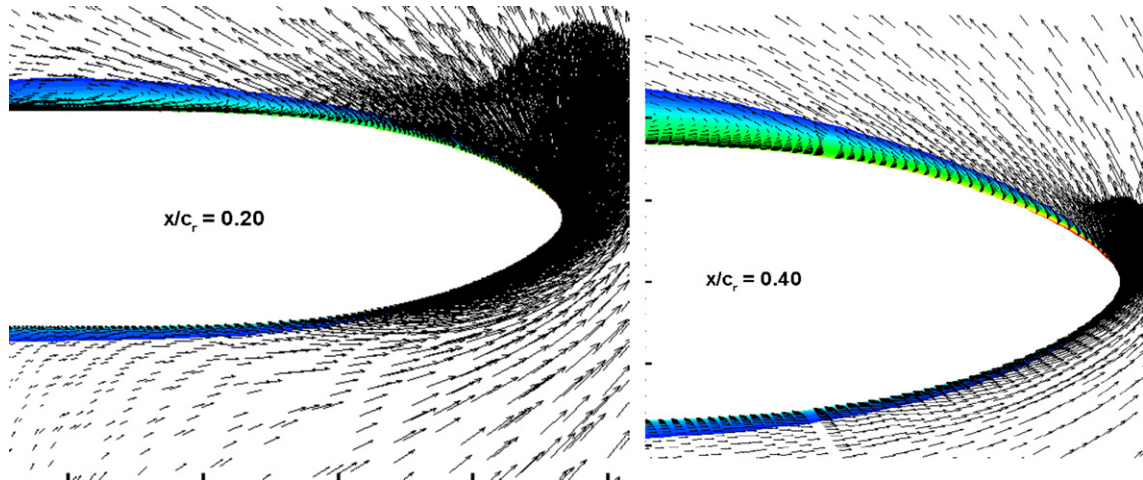


Fig. 12. Velocity vectors and total pressure loss contours in two cross sections for case 4.5 ($M = 0.4$, $Re = 3 \times 10^6$, $\alpha = 13^\circ$). (For interpretation of the references to color in this figure, the reader is referred to the web version of this article.)

The situation at the cross section $x/c_r = 0.60$ and $x/c_r = 0.65$ is shown in Fig. 14. At $x/c_r = 0.6$ there is a double branched vortex and at $x/c_r = 0.6$ there are finally two separate vortices. The inner vortex is much weaker than the outer one, but has the same dimension. From this position ($x/c_r = 0.6$), the inner vortex has no longer a connection to the leading edge and thus it is no longer fed. The outer vortex is fed by the leading edge and thus further growing.

The spatial development of the two vortices is shown in Fig. 15 by 3-D stream traces. The volume ribbons are colored by the local C_p values. The volume ribbons are generated by placing rakes into the vortex cores and in the boundary layer region at the wing apex, then tracing the ribbons in upstream and downstream direction. By their twist the ribbons also indicate the local vorticity. At the foremost part of the wing, the flow passes the leading edge with little vorticity and then runs along the inner wing surface towards the trailing edge (left-hand side of Fig. 15). More downstream along the leading edge the vorticity in the boundary layer increases and the flow particles are bound to the inner vortex. The close up at the right-hand side of Fig. 15 shows the onset of the main primary vortex. There is a region, where the primary separation already exists, but the inner vortex still gets flow material from the outer flow. As soon as the primary vortex gets certain strength, the inner vortex no longer gets material from the outer flow.

During the VFE-2 experiments at TUM [9], it was seen that this inner vortex varies considerably with a decrease of the Reynolds number. Surface visualizations by oil flow pattern at $Re = 1$ Mio have shown a much more inboard position and an earlier onset of the inner vortex as shown in Fig. 8. For a better understanding of this effect, the variation of the Reynolds number was also investigated numerically.

Fig. 16 shows the effect of the decreasing Reynolds number in the surface pressure contours. (The Mach number was kept constant, only the Reynolds number was changed in the calculations.) As the figure indicates, the smaller the Reynolds number gets, the more upstream moves the primary separation and in turn the earlier begins the inner vortex and the weaker it gets.

In the 3-D flow structure, which is shown in Fig. 17 by means of total pressure loss contours, the impact of the decreasing Reynolds number can be seen very clearly. With the upstream moving primary separation the origin of the inner vortex also moves upstream and its axis moves more inboard. Between $Re = 2$ Mio and $Re = 3$ Mio there are only small differences, but at

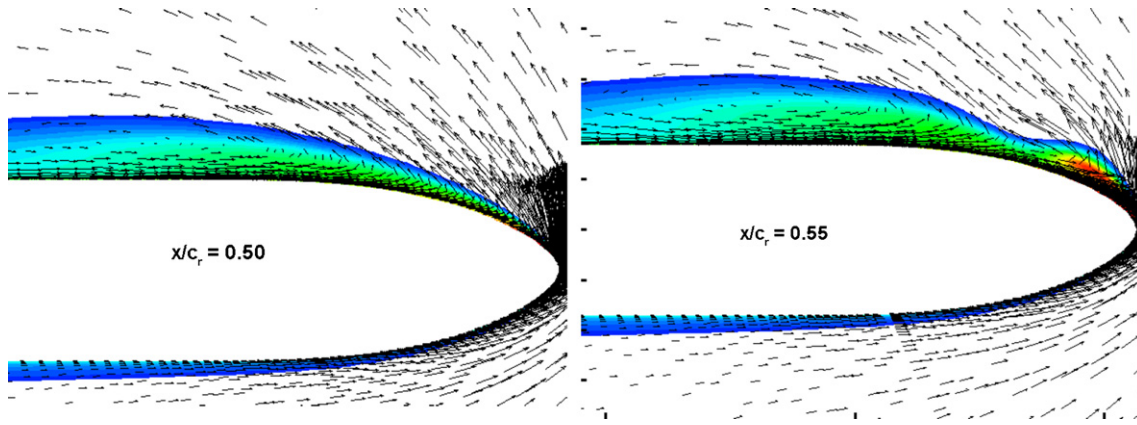


Fig. 13. Velocity vectors and total pressure loss contours in two cross sections for case 4.5 ($M = 0.4$, $Re = 3 \times 10^6$, $\alpha = 13^\circ$).

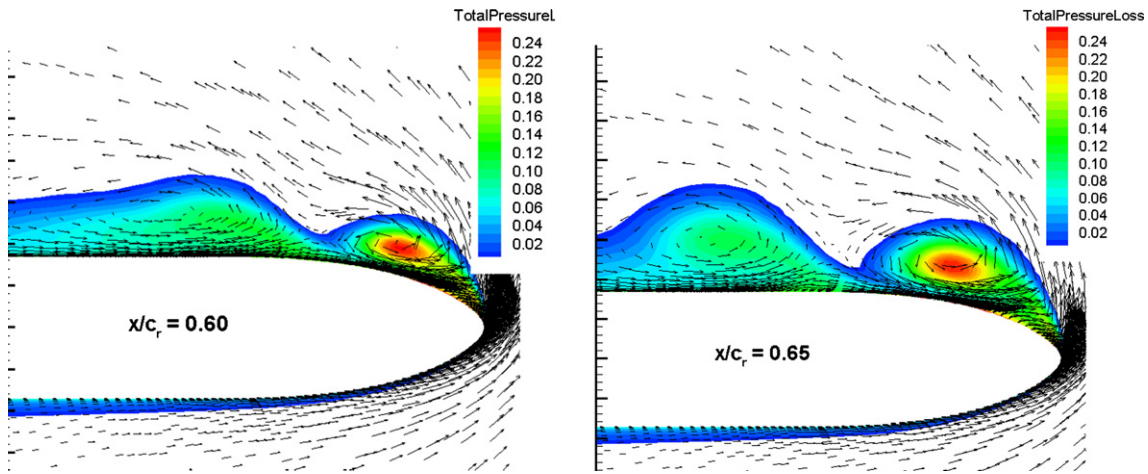


Fig. 14. Velocity vectors and total pressure loss contours in two cross sections for case 4.5 ($M = 0.4$, $Re = 3 \times 10^6$, $\alpha = 13^\circ$).

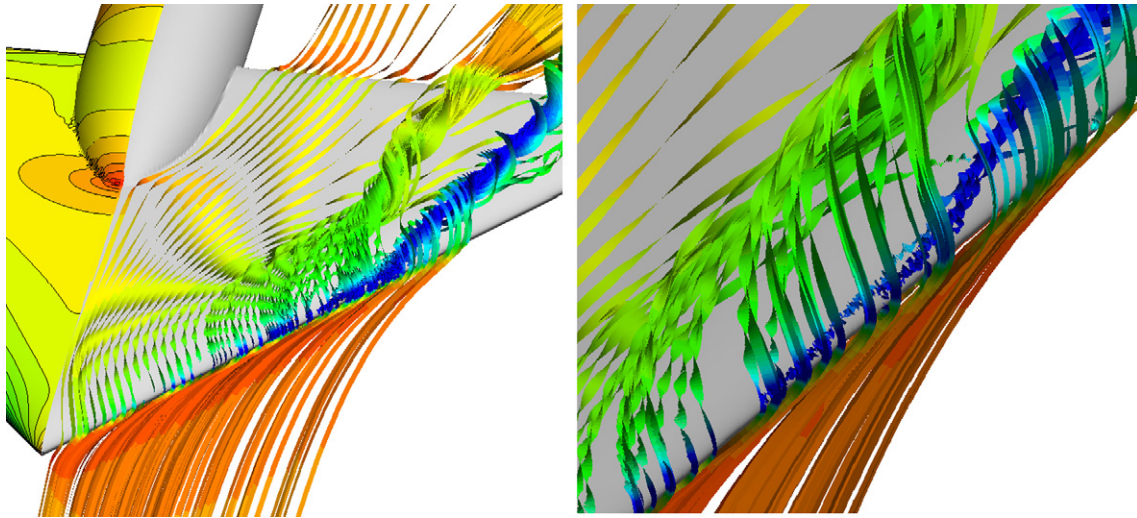


Fig. 15. 3-D flow features (stream traces by 3-volume ribbons) for case 4.5 ($M = 0.4$, $Re = 3 \times 10^6$, $\alpha = 13^\circ$).

$Re = 1$ Mio, there is a considerable inboard shift of the inner vortex.

4.4. Test case 14, $M = 0.4$, $Re = 6 \times 10^6$, $\alpha = 18^\circ$

This test case is again the round leading edge geometry, but at a higher angle of attack. The leading edge separation now moves close to the wing apex and the inner vortex has no considerable ef-

fect. A fully developed primary vortex without vortex break down should be expected for this case. The vortical flow structure is shown in Fig. 18 and is visualized again by 3-D volume ribbons. There is a separation at the apex region of the wing which rolls up into a small inner vortex. But this inner vortex only has a small impact on the pressure distribution in the apex region. The leading edge separation now begins very close to the wing apex. The core of the leading edge vortex remains very compact until $x/c_r = 0.8$.

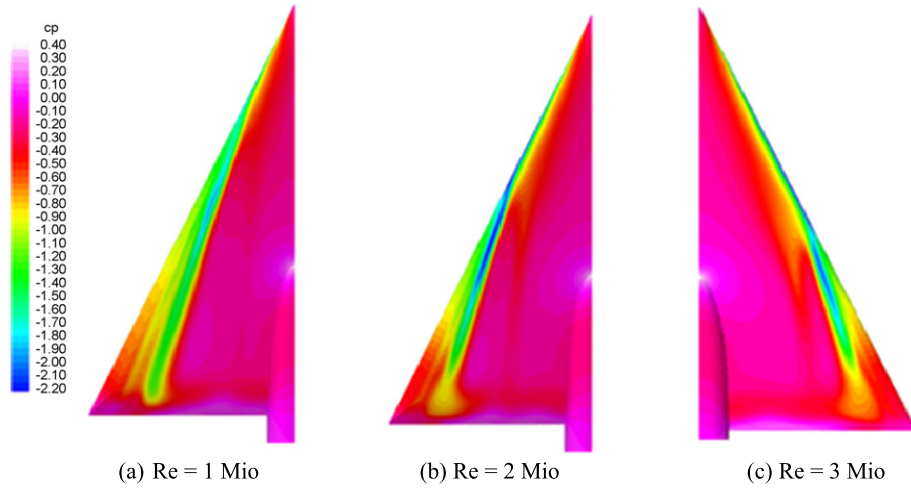


Fig. 16. Effect of decreasing Reynolds number on surface pressure contours for case 4.5 ($M = 0.4$, $Re = 3 \times 10^6$, $\alpha = 13^\circ$).

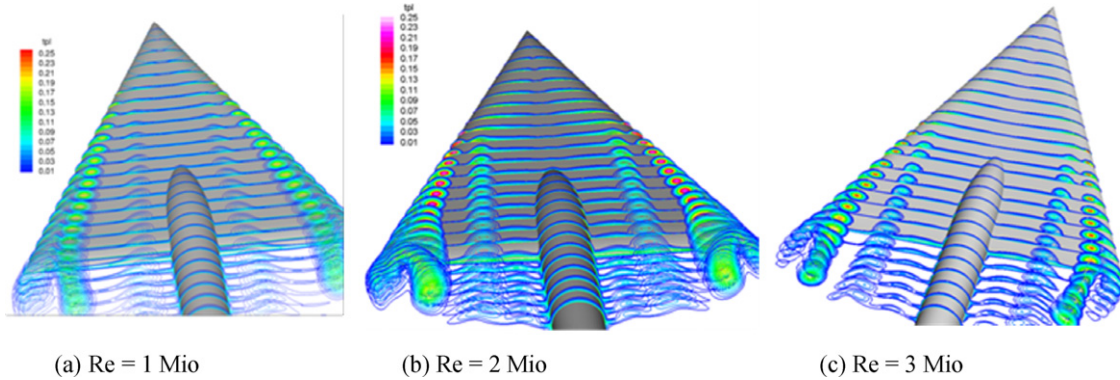


Fig. 17. Effect of decreasing Reynolds number for case 4.5 ($M = 0.4$, $Re = 3 \times 10^6$, $\alpha = 13^\circ$). Total pressure loss contours at different cross sections.

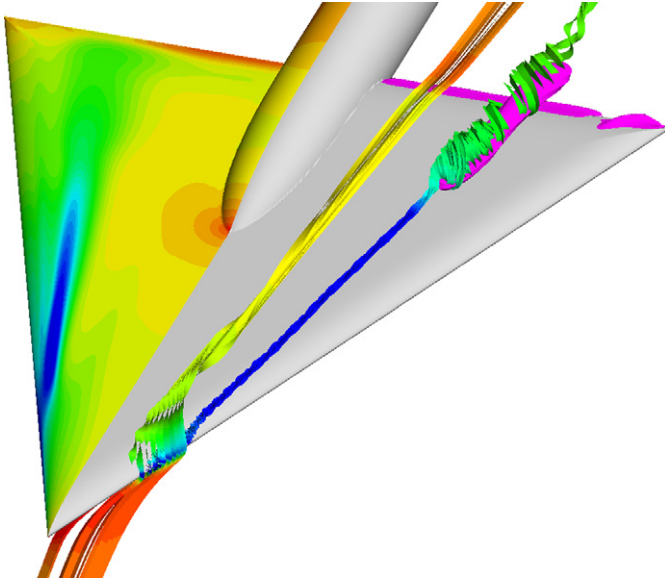


Fig. 18. 3-D flow features (stream traces by 3-volume ribbons) for case 14 ($M = 0.4$, $Re = 6 \times 10^6$, $\alpha = 18^\circ$). (For interpretation of the references to color in this figure, the reader is referred to the web version of this article.)

At this position the core forms a small bubble until to the rear end of the wing where the core becomes compact again. The pink colored bubble in the figure is an iso-surface of zero axial velocity. Inside the bubble the axial velocity is negative and outside it is

positive. Negative axial velocity in the vortex core is a criterion for vortex breakdown, which means that the calculation shows a very weak vortex breakdown. In general for a 65° swept delta wing, vortex breakdown is expected at $\alpha \geq 21^\circ$, but the geometry has a highly curved trailing edge region, which induces an additional increase in pressure. This may lead to an earlier vortex breakdown at the very rear end of the wing. Another reason may be an underprediction of the axial velocity in the numerical calculation due to still existing defects for vortical flow in the actual turbulence model. This earlier vortex break down was also observed in some other numerical solutions [8].

Fig. 19 shows the surface pressure contours compared with the NASA LTPT experiments [2]. The leading edge separation has now moved upstream, very close to the wing apex and thus there is less boundary layer material which can form the inner vortex. The inner vortex is consequently very weak in the calculation (Fig. 19a). In the experimental pressure distributions (Fig. 19b) there is a rather compact suction peak up to $x/c_r = 0.8$. At $x/c_r = 0.95$, there is still a vortical flow structure, but the suction peak is smeared out. This may indicate a very weak vortex breakdown at the rear end of the wing (due to the high curvature of the trailing edge).

A detailed comparison of the surface pressure distribution with the NASA experiments [2] is given in (Fig. 20). Essential differences are at $x/c_r = 0.2$. The numerical solution does not yet show a primary vortex, whereas the experiment shows already a primary vortex and also an inner vortex in this cross section. Again, the numerical solution predicts the primary separation slightly more downstream as it is in the experiment.

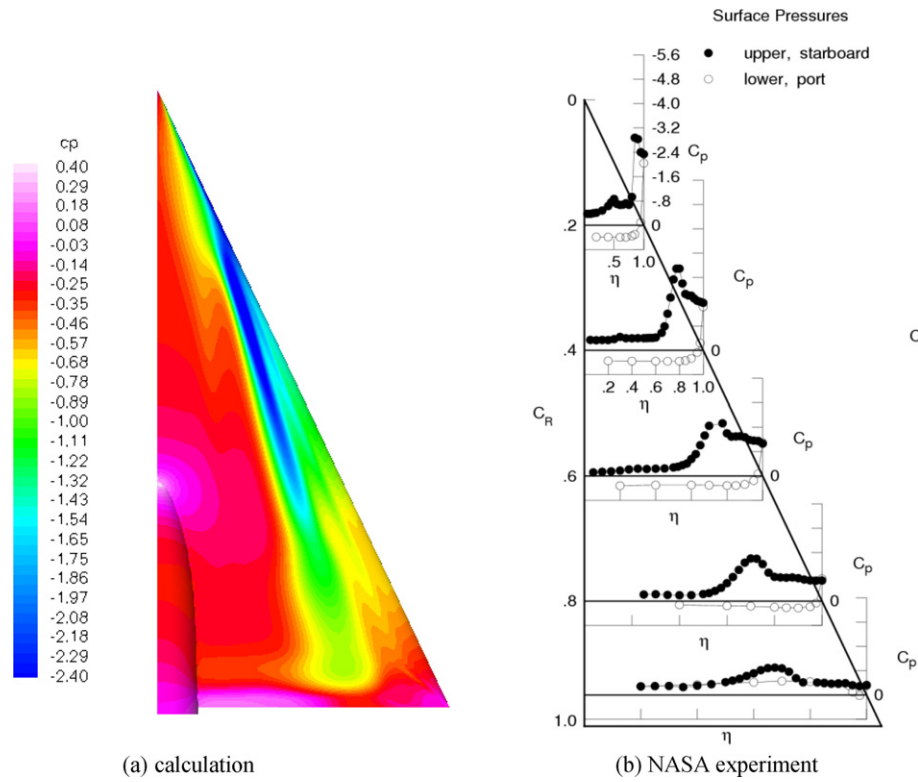


Fig. 19. Comparison of numerical surface pressure contours with experimental data for case 18 ($M = 0.4$, $Re = 6 \times 10^6$, $\alpha = 18^\circ$).

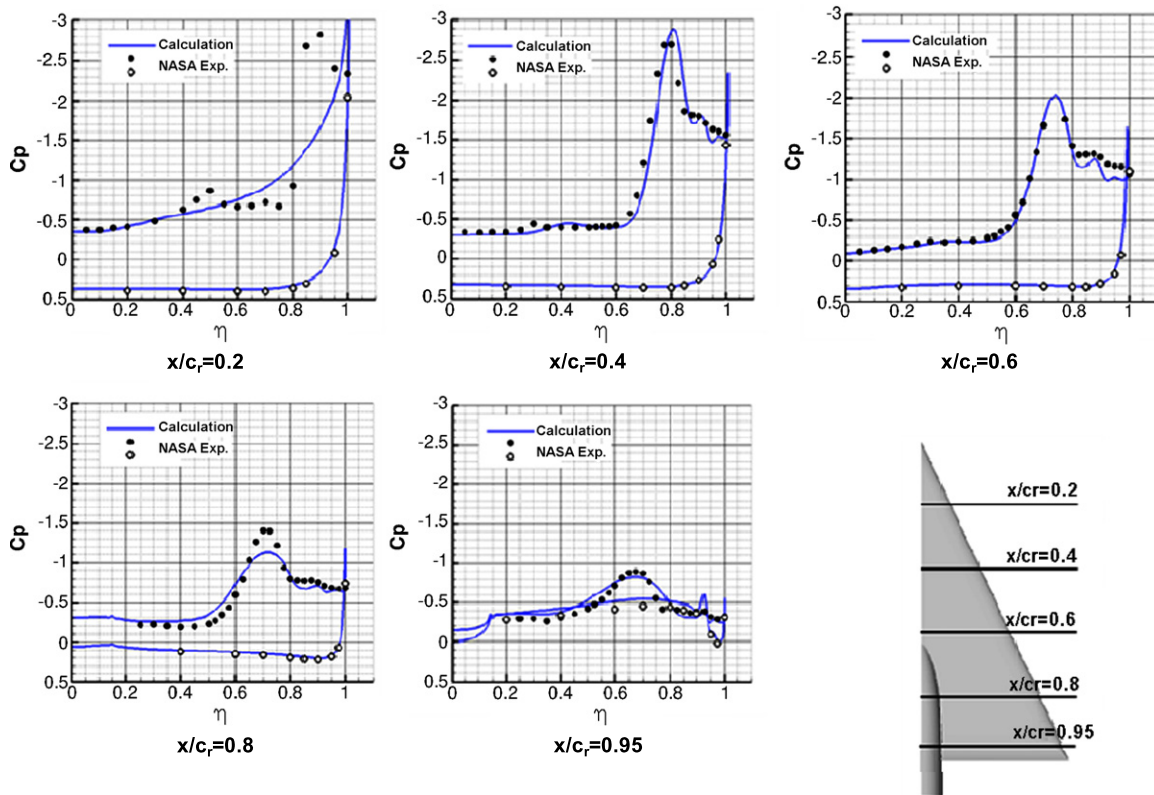


Fig. 20. Comparison of numerical and experimental surface pressure distributions for case 14 ($M = 0.4$, $Re = 6 \times 10^6$, $\alpha = 18^\circ$).

At $x/c_r = 0.4$ and $x/c_r = 0.6$ the numerical solution shows the correct flow features. There is a dominating primary vortex and the effect of a secondary vortex (between the leading edge and suc-

tion peak). Differences between calculation and experiments occur again in the region of the secondary vortex and are typical for RANS solutions. At $x/c_r = 0.8$ the numerical solutions is under-

predicting the main suction peak and smearing it out. The reason therefore may be the above mentioned spread of the vortex core. At the cross section $x/c_r = 0.95$ the calculation with its weak vortex breakdown matches quite well to the experimental data. This indicates that the above mentioned weak vortex breakdown due to the high curvature of the rear end of the wing is also present in the experiment.

5. Conclusion

For a delta wing with a rounded leading edge, the prediction of the onset of the primary leading edge separation is the most essential problem. The position of this separation point can be predicted too much upstream or too much downstream or (by accident?) at the correct position. Depending on this, the agreement between numerical and experimental results can be very good or less good. One uncertainty parameter which was found for these test cases is the unknown transition, which can have a strong effect on the solution. So transition modeling should be further promoted. Another difficulty is the effect of the Reynolds number at delta wings with round leading edges. This effect also can be under- or over-predicted.

At higher incidence, the correct prediction of vortex break down is also a very difficult task. In the numerical solution, vortex break down occurred at earlier angles of attack compared to the experiment. This may be due to an under-prediction of the axial velocity in the vortex core. Either there is still a deficit of the existing turbulence models for a proper treatment of vortical flow, or RANS methods are overstrained and DES methods are required for the correct prediction of vortex break down.

Summarizing it can be stated, that not for all presented test cases the experimental results could be predicted in detail correctly, but anyhow detailed numerical flow analysis gave an essential insight into the complex flow structure of the double vortex system at round LE and the numerical calculations helped to design the PIV experiments.

Acknowledgements

The guidance and encouragement of Prof. Dietrich Hummel was instrumental in the completion of this work, for which the author is grateful. The author also would like to thank the experimental researchers within the VFE-2 group who provided experimental data for this paper.

References

- [1] K. Chiba, S. Obayashi, CFD visualization of second primary vortex structure on a 65-degree delta wing, AIAA Paper 2004-1231, Jan. 2004.
- [2] J. Chu, J.M. Luckring, Experimental surface pressure data obtained on 65° delta wing across Reynolds number and Mach number ranges, NASA TM 4645, 1996.
- [3] F. Coton, S. Mat, R. Galbraith, Low speed wind tunnel characterization of the VFE-2 wing, AIAA Paper 2008-0382, January 2008.
- [4] S. Crippa, Steady, subsonic CFD analysis of the VFE-2 configuration and comparison to wind tunnel data, AIAA Paper 2008-0397, Jan. 2008.
- [5] R.M. Cummings, A. Schütte, Detached-eddy simulation of the vortical flowfield about the VFE-2 delta wing, AIAA Paper 2008-0396, Jan. 2008.
- [6] G. Drougge, The international vortex flow experiment for computer code validation, in: ICAS Proceedings, vol. 1, 1988, pp. 35–41.
- [7] J.A. Ekaterinaris, L.B. Schiff, Numerical simulation of incidence and sweep effects on delta wing vortex breakdown, Journal of Aircraft 31 (5) (1994) 1043–1049.
- [8] W. Fritz, R.M. Cummings, What was learned from the numerical simulations for the VFE-2, AIAA Paper 2008-0399, Jan. 2008.
- [9] A. Furman, C. Breitsamter, Turbulent and unsteady flow characteristics of delta wing vortex systems, AIAA Paper 2008-0381, January 2008.
- [10] E. Gurdamar, Influence of grid resolution on the accuracy of high angle of attack delta wing simulations, AIAA Paper 2008-0394, Jan. 2008.
- [11] D. Hummel, The second international vortex flow experiment (VFE-2): Objective and first results, in: 2nd International Symposium on Integrating CFD and Experiments in Aerodynamics, Cranfield University, 2005.
- [12] D. Hummel, Review of the second international vortex flow experiment (VFE-2), AIAA Paper 2008-0377, Jan. 2008.
- [13] D. Hummel, G. Redeker, A new vortex flow experiment for computer code validation, in: RTO AVT Symposium Vortex Flow and High Angle of Attack Aerodynamics, Loen, Norway, 7–11 May 2001, Meeting Proceedings RTO-MP-06(1), SYA 8-1 to 8-31, 2003.
- [14] R. Konrath, C. Klein, R.H. Engler, D. Otter, Analysis of PSP results obtained for the VFE-2 65° delta wing configuration at subsonic and transonic speed, AIAA Paper 2006-0060, 2006.
- [15] R. Konrath, C. Klein, A. Schröder, PSP and PIV investigations on the VFE-2 configuration in sub- and transonic flow, AIAA Paper 2008-0379, January 2008.
- [16] N. Kroll, P. Aumann, W. Bartelheimer, H. Bleecke, B. Eisfeld, J. Lieser, R. Heinrich, M. Kuntz, E. Monsen, J. Raddatz, U. Reisch, B. Roll, Flower installation and user handbook, DLR Doc. Nr. MEGAFLOW-1001, 1998.
- [17] J. Le Roy, O. Rodriguez, Experimental and CFD contribution to understanding delta wing vortical flow, AIAA Paper 2008-0380, January 2008.
- [18] J.M. Luckring, Reynolds number and leading-edge bluntness effects on a 65° delta wing, AIAA Paper 2002-0419, 2002.
- [19] J.M. Luckring, Transonic Reynolds number and leading-edge bluntness effects on a 65° delta wing, AIAA Paper 2003-0753, 2003.
- [20] J.M. Luckring, Compressibility and leading-edge bluntness effects for a 65° delta wing, AIAA Paper 2004-0765, 2004.
- [21] J.M. Luckring, Reynolds number, compressibility, and leading-edge bluntness effects on delta-wing aerodynamics, in: ICAS Proceedings Yokohama 2004, Paper 4.1.4, 2004.
- [22] J.M. Luckring, Initial experiments and analysis of vortex flow on blunt edge delta wings, AIAA Paper 2008-378, January 2008.
- [23] A.M. Mitchell, S.A. Morton, J.R. Forsythe, R.M. Cummings, Analysis of delta-wing vortical substructures using detached-eddy simulation, AIAA Journal 44 (5) (2006) 964–972.
- [24] L. Schiavetta, O.J. Boelens, S. Crippa, R.M. Cummings, W. Fritz, K.J. Badcock, Shock effects on delta wing vortex breakdown, AIAA Paper 2008-0395, Jan. 2008.
- [25] A. Schütte, H. Lüdeke, Numerical investigations on the VFE-2 rounded leading edge configuration using the unstructured DLR TAU code, AIAA Paper 2008-0398, Jan. 2008.